Unified Frequency-Domain Analysis of Switched-Series-RC Passive Mixers and Samplers

Michiel C. M. Soer, *Student Member, IEEE*, Eric A. M. Klumperink, *Senior Member, IEEE*, Pieter-Tjerk de Boer, Frank E. van Vliet, *Senior Member, IEEE*, and Bram Nauta, *Fellow, IEEE*

***Abstract*—A wide variety of voltage mixers and samplers are implemented with similar circuits employing switches, resistors, and capacitors. Restrictions on duty cycle, bandwidth, or output frequency are commonly used to obtain an analytical expression for the response of these circuits. This paper derives unified expressions without these restrictions. To this end, the circuits are decomposed into a polyphase multipath combination of single-ended or differential switched-series-RC kernels. Linear periodically time-variant network theory is used to find the harmonic transfer functions of the kernels and the effect of polyphase multipath combining. From the resulting transfer functions, the conversion gain, output noise, and noise figure can be calculated for arbitrary duty cycle, bandwidth, and output frequency. Applied to a circuit, the equations provide a mathematical basis for a clear distinction between a "mixing" and a "sampling" operating region while also covering the design space "in between." Circuit simulations and a comparison with mixers published in literature are performed to support the analysis.**

***Index Terms*—Frequency conversion, linear periodically time variant (LPTV), low noise, noise folding, passive mixing, voltage sampling**

I. Introduction

In radio front ends, mixers normally perform frequency conversion, with continuous-time input and output signals. Samplers convert a continuous-time input into a discrete-time output signal but can also provide frequency conversions (aliasing). Mixing and sampling seem to be quite different functions and are analyzed differently but can be implemented by similar circuits. Some examples are shown in Fig. 1.

The basic building block of these circuits consists of a resistor and a capacitor in series, which are switched to the input voltage $V_{\rm in}$. As there is no parallel resistance across the capacitance when the switch is off, the capacitor holds its charge in the OFF state. The circuits are purely passive because the switches act as time-variant resistances and no power gain is possible. Still, the passive circuits in Fig. 1 have very interesting properties, like very high linearity [1], upconversion of a low-pass baseband filter into an RF bandpass filter [2], and the possibility to cancel local oscillator (LO) harmonics [3]. We will analyze the transfer function and noise of these circuits in this paper assuming a perfect hold operation. Thus, the analysis does not hold for circuits with a (low) resistor in parallel to the capacitor [4], which is also often used in "current-driven" passive mixers [5]–[7]. Moreover, charge sampling [8] circuits are not covered, as they periodically short circuit the capacitors and dump the capacitor charge to ground.

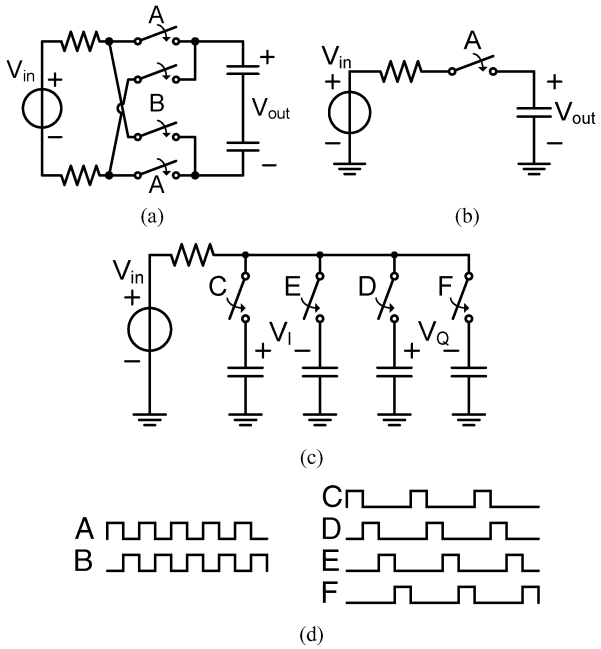

Fig. 1. Switched-RC application examples. (a) Switching mixer. (b) Sampling mixer/track and hold. (c) In-phase/Quadrature mixer with (d) polyphase clocks A–F.

Individual switched-series-RC circuits have been analyzed individually in literature by posing restrictions on the design parameters. The differential (DI) switching mixer [Fig. 1(a)] has a fixed 50% duty cycle [9]. The switched RC in Fig. 1(b) is not only in use as a sampling mixer [10], [11] but also as a track-and-hold sampler [12]. In both cases, the RC time is considered to be infinitely small. The conversion gain and noise figure (NF) for the I/Q image reject mixer [Fig. 1(c)] as proposed by Tayloe [13] have only been calculated for dc output frequency [14].

In this paper, we propose a unified frequency-domain analysis that can be applied to *all* of these switched-series-RC circuits and for arbitrary duty cycle, RC time, and output frequency. In a two-step approach, we will combine single-state building blocks, called kernels, with polyphase clocking into multistate systems. The first step investigates the effect of combining the outputs of multiple kernels, switched with polyphase clocks. In the second step, the precise behavior of a single kernel is

Manuscript received October 01, 2009; revised January 18, 2010; accepted March 04, 2010. This paper was recommended by Associate Editor A. J. Lopez Martin.

M. C. M. Soer, E. A. M. Klumperink, and B. Nauta are with the Integrated Circuit Design Group, Centre for Telematics and Information Technology (CTIT), University of Twente (UT), 7500 AE Enschede, The Netherlands (e-mail: m.c.m.soer@utwente.nl; e.a.m.klumperink@utwente.nl; b.nauta@utwente.nl).

P.-T. de Boer is with the Design and Analysis of Communication Systems Group, CTIT, UT, 7500 AE Enschede, The Netherlands (e-mail: ptdeboer@cs.utwente.nl).

F. E. van Vliet is with Netherlands Organization for Applied Scientific Research (TNO), 2509 JG The Hague, The Netherlands, and also with the Integrated Circuit Design Group, CTIT, UT, 7500 AE Enschede, The Netherlands (e-mail: frank.vanvliet@tno.nl).

Digital Object Identifier 10.1109/TCSI.2010.2046968

analyzed. The switching nature of the networks requires us to use linear periodically time-variant (LPTV), instead of linear time-invariant (LTI), network theory.

First, in Section II, the notation used for LPTV systems is summarized. In Section III, the decomposition into polyphase kernels is qualitatively explained. The effect of polyphase combining is covered in Section IV. Section V performs the LPTV analysis on single-ended (SE) and DI kernels to find the kernel harmonic transfer functions (HTFs). In Section VI, the design space is divided into "sampling" and "mixing" regions, for which approximate gain and noise equations are derived. The theoretical results are applied to an application example in Section VII, while conclusions are presented in Section VIII.

II. LPTV Systems

For an LPTV network, the output spectrum V_o is a summation of an infinite number of frequency-shifted and filtered input spectra V_i [10]

$$V_o(f_o) = \sum_{n=-\infty}^{\infty} H_n(f_o) V_i(f_o - n f_s) \tag{1}$$

where $f_s = 1/T_s$ is the frequency for which the system is periodic, $H_n(f_o)$'s are the HTFs, n is the harmonic index, and f_o is the frequency at the output. Each HTF is the transfer function for the frequency shift nf_s. For the argument of V_i, the shorthand notation for the input frequency is introduced as

$$f_i \equiv f_o - n f_s. \tag{2}$$

For random signals, the relation between the input power spectral density (PSD) N_i and the output PSD N_o in LPTV systems is [15]

$$N_o(f_o) = \sum_{n=-\infty}^{\infty} |H_n(f_o)|^2 N_i(f_o - n f_s). \tag{3}$$

One of the HTFs H_n, with index $n = w$, renders the desired frequency conversion. Usually, for a downconversion mixer, $w = -1$, and for Nyquist sampling, $w = 0$. The conversion gain $CG_w(f_o)$ depends upon w such that

$$CG_w(f_o) = H_w(f_o). \tag{4}$$

The single sideband NF also depends on w

$$\begin{aligned} F_w(f_o) &= \frac{SNR_{\text{in}}}{SNR_{\text{out}}} = \frac{N_o(f_o) + N_{o,\text{int}}(f_o)}{N_i(f_o - w f_s)} \cdot \frac{1}{|CG_w(f_o)|^2} \\ NF_w(f_o) &= 10 \log\left(F_w(f_o)\right) \end{aligned} \tag{5}$$

where $N_{o,\text{int}}(f_o)$ is the output noise PSD due to internal noise sources.

III. Decomposition Into Polyphase Kernels

The circuits in Fig. 1 share the following properties.

1) The capacitor voltages are the circuit states.
2) The output voltage is a combination of states.
3) The clocks are polyphase.

A set of clocks is polyphase if they have the same duty cycle and start at regularly spaced intervals within the period time. The clocks are not allowed to overlap when high. Familiar examples to combine output voltages include the following.

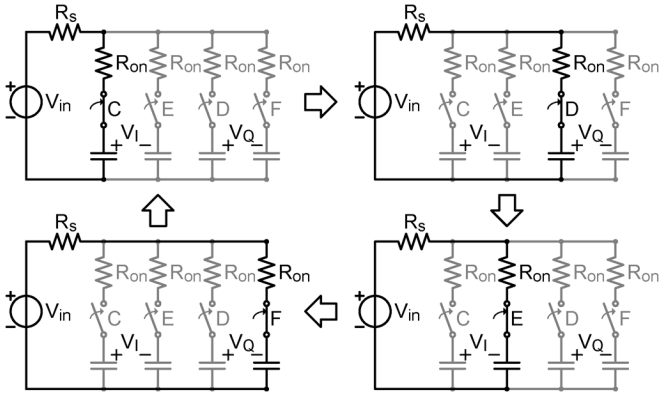

Fig. 2. Polyphase SE kernel example.

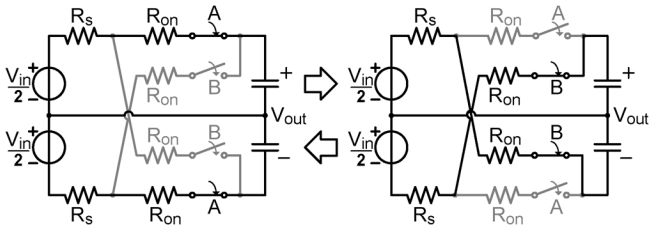

Fig. 3. Polyphase DI kernel example.

1) Subtract outputs to cancel even LO harmonics [Fig. 1(a)].
2) Take in-phase and quadrature outputs for image rejection [Fig. 1(c)].

An increasing number of states increase the complexity of the LPTV analysis. However, because the clocks do not overlap, the capacitor voltages (the circuit states) are independent. Therefore, we apply a two-step approach.

1) Calculate the effect of combining the capacitor voltages in a polyphase system (Section IV).
2) Calculate the transfer to a single capacitor voltage with a single-state LPTV calculation (Section V).

With this approach, the combination of basic single-state building blocks (kernels) into complex multistate systems is possible.

A. SE and DI Kernel Examples

To clarify the polyphase kernel concept, the I/Q mixer in Fig. 1(c) is plotted step by step in Fig. 2. The switches are modeled with infinite off-resistance and finite on-resistance R_{on}. The source is characterized by the resistance R_s. During each of the switch intervals, there is a single current loop flowing from the source through R_s and R_{on} into the capacitor and back to the source. For calculating the transfer function, R_s and R_{on} can be replaced by the equivalent series resistance

$$R = R_s + R_{\text{on}}. \tag{6}$$

Analysis of this current loop, defined as the SE kernel, is sufficient to find the capacitor voltage.

For DI inputs, a second kernel is needed, as the example in Fig. 3 shows. Here, a capacitor is connected to the input *twice* in each period. Compared to the SE kernel [Fig. 4(a)], in the definition of the DI kernel [Fig. 4(b)], the second switch is delayed half a period after the first switch and has the same duty cycle.

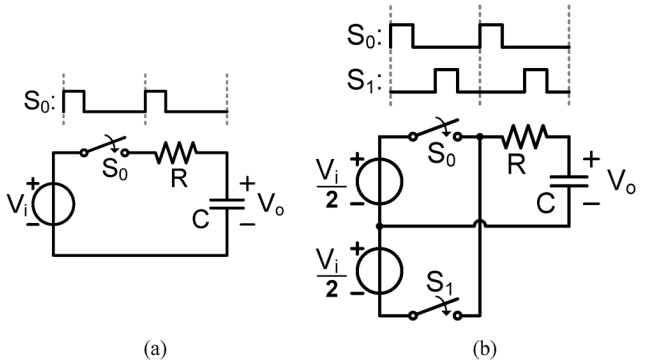

(a) (b)

Fig. 4. (a) SE kernel and (b) DI kernel; S_0 and S_1 have duty cycle D.

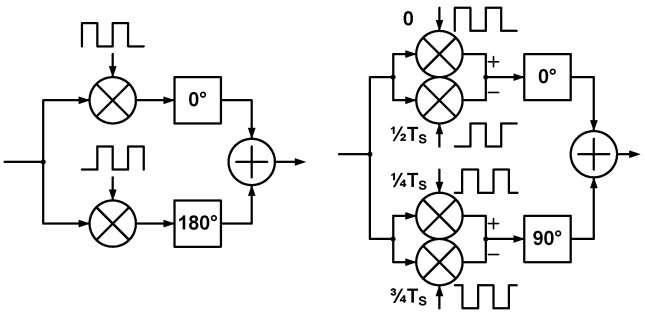

(a) (b)

Fig. 5. Polyphase multipath example (a) with $L = 2$ and $D = 50\%$ and (b) with $L = 4$ and $D = 50\%$.

B. Kernel NF

In the kernels, the noise contributions from resistors R_s and R_{on} can be represented by an equivalent noise source with white PSD N_i and N_{int}. The ratio between the noise powers is equal to the ratio in resistance

$$\frac{N_{\text{int}}}{N_i} = \frac{R_{\text{on}}}{R_s}. \tag{7}$$

Both of these equivalent voltage noise sources appear in series with the resistors and can be moved in the loop toward the input voltage source. Applying this to (3)–(5) results in a simpler expression for the kernel NF

$$F_w(f_o) = \underbrace{\left(1 + \frac{R_{\text{on}}}{R_s}\right)}_{\text{A}} \cdot \underbrace{\frac{\sum_{n=-\infty}^{\infty} |H_n(f_o)|^2}{|H_w(f_o)|^2}}_{\text{B}}. \tag{8}$$

Part A corresponds to the LTI NF for the SE kernel with closed switch. Part B represents the noise folding due to the circuit switching.

Therefore, for calculating the NF, the LPTV kernel analysis can be done with the total resistance R, and the effect of R_{on} can be factored in afterward.

IV. Polyphase Multipath Systems

First, the effect of combining multiple kernels in a polyphase multipath system is studied. Two familiar examples of a polyphase system are as follows:

1) DI mixer [Fig. 5(a)]; ,
2) Hartley image rejection mixer [Fig. 5(b)].

In general, an L-path polyphase system has L independent parallel LPTV circuits (with HTFs H_n) driven by a clock shifted $l \cdot (T_s/L)$ in time, where l is the path number. Before combining, each path is phase shifted with $-w \cdot l \cdot 360°/L$, where w indicates the desired frequency shift ($w = -1$ for the examples). The signal contributions of all paths are then summed into a single output. The effects of such a system on deterministic signals and random noise are examined in this section.

A. Signals

From Fourier analysis, it is known that shifting a signal in time causes a linear phase shift in the frequency domain. Mathematically, if the time shift is σ_d, the Fourier pair of signal v is

$$v(t - \sigma_d) \overset{\mathcal{F}}{\leftrightarrow} V(f) e^{-j2\pi f \sigma_d}. \tag{9}$$

For an LPTV system with HTFs H_n, shifting the switching moments in time has the same effect as shifting the input and output in the opposite time direction

$$\begin{aligned} v_i(t + \sigma_d) &\overset{\mathcal{F}}{\leftrightarrow} V_i(f_i) e^{j2\pi f_i \sigma_d} \\ v_o(t + \sigma_d) &\overset{\mathcal{F}}{\leftrightarrow} V_o(f_o) e^{j2\pi f_o \sigma_d} \\ V_o(f_o) e^{j2\pi f_o \sigma_d} &= \sum_{n=-\infty}^{\infty} H_n(f_o) V_i(f_o - n f_s) e^{j2\pi (f_o - n f_s)\sigma_d}. \end{aligned} \tag{10}$$

Bringing the phase terms together

$$V_o(f_o) = \sum_{n=-\infty}^{\infty} H_n(f_o) e^{-j2\pi n f_s \sigma_d} V_i(f_o - n f_s). \tag{11}$$

The HTFs get a phase term that is equal to $e^{-j2\pi n f_s \sigma_d}$ when the switching moments are shifted forward by σ_d in time. Therefore, the lth path has a phase shift of $n \cdot l \cdot 360°/L$ due to the delayed clocking.

Together with the phase shifter blocks, each path l has the total phase term

$$e^{-j2\pi n l/L} e^{j2\pi w l/L} = e^{-j2\pi (n-w) l/L}. \tag{12}$$

Summing the signals of all paths gives the HTFs of the total system

$$\begin{aligned} H_{n,\text{polyphase}}(f_o) &= \sum_{l=0}^{L-1} H_n(f_o) e^{-j2\pi (n-w) l/L} \\ &= \begin{cases} 0, & \frac{n-w}{L} \neq \text{integer} \\ L \cdot H_n(f_o), & \frac{n-w}{L} = \text{integer}. \end{cases} \end{aligned} \tag{13}$$

Therefore, a polyphase multipath system yields a processing gain of L for all frequency shifts satisfying

$$n = i \cdot L + w, \qquad \text{where } i = \ldots, -2, -1, 0, 1, 2, \ldots \tag{14}$$

while the transfer functions for all other frequency shifts are zero. For example, with $L = 2$ and $w = -1$, this results in cancellation for all $n = \ldots, -2, 0, 2, \ldots$. For all $L > 2$, either n or $-n$ or both are canceled, resulting in image rejection.

B. Noise

For a comparison between the noise PSD of a single kernel and L kernels combined in a polyphase manner, regard the

example in Fig. 2. We observe the following for a polyphase system.

1) Each path has a separate $R_{\rm on}$.
2) R_s is connected to the paths at different intervals.

The multiple $R_{\rm on}$'s are physically separate resistances, so their noise is completely uncorrelated. The polyphase combination will add the noise powers so that the output noise due to $R_{\rm on}$ increases with the number of paths L.

The source resistance R_s is shared between paths but is never connected to several paths at the same time. Assuming white noise, the noise voltage at one time is completely uncorrelated to the noise voltage at a different time. Because the polyphase clocks do not overlap, the noise powers due to R_s will also be uncorrelated and will add in power.

As a consequence, the polyphase system noise is L times the noise of a kernel alone

$$N_{o,\rm polyphase} = N_{o,\rm kernel} \cdot L \tag{15}$$

where $N_{o,\rm kernel}$ is calculated with (3). From (13), the signal power is

$$S_{o,\rm polyphase} = S_{o,\rm kernel} \cdot L^2. \tag{16}$$

Then, according to (5)

$$F_{\rm polyphase} = \frac{F_{\rm kernel}}{L}. \tag{17}$$

Adding polyphase paths lowers the NF as long as the clocks do not overlap.

V. Kernels

Section III defined two kernels (shown in Fig. 4) that are sufficient to find the transfer function to each of the capacitor voltages. In this section, the HTFs of the kernels are first qualitatively described to provide intuitive insight and then exactly derived.

A. Qualitative Analysis

The kernels have only two degrees of freedom: the duty cycle D and the RC time associated with the resistor and capacitor. The RC bandwidth is defined as

$$f_{rc} \equiv \frac{1}{2\pi RC}. \tag{18}$$

For duty cycle D, the switch will be closed for time $D \cdot T_s$. The ratio between the switch-on time and the RC-time constant will be designated with Γ

$$\Gamma \equiv \frac{DT_s}{RC} = 2\pi D \frac{f_{rc}}{f_s}. \tag{19}$$

For large Γ, the output voltage will settle to the input voltage during the switch-on time. For small Γ, the output has no time to settle. The value of Γ will therefore influence the response of the circuit, and we can define two regions with $\Gamma = 2$ as the border. The choice for this particular border (as opposed to $\Gamma = 1$ or any other value) is motivated at the end of Section VI-C.

When the RC-time constant is relatively small ($\Gamma \gg 2$), the behavior of the circuit can be understood by looking at the node voltages (the Thevenin equivalent in Fig. 6). When the switch is closed, the capacitor voltage will follow the input, and when the switch is open, the last voltage will be held on the capacitor.

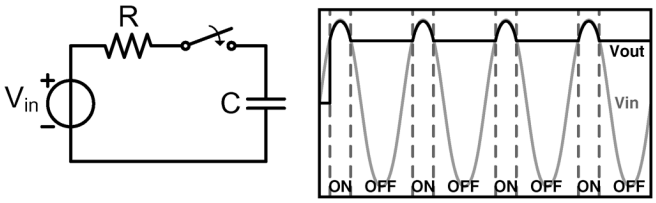

(a) (b)

Fig. 6. SE kernel (a) Thevenin equivalent with (b) waveform example for $\Gamma \gg 2$.

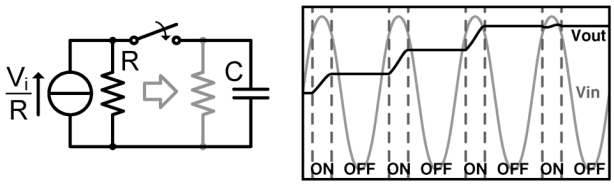

(a) (b)

Fig. 7. SE kernel (a) Norton equivalent with (b) waveform example for $\Gamma \ll 2$.

Such operation is commonly referred to as track and hold and is widely used in samplers. Therefore, *the part of the design space for which* $\Gamma \gg 2$ *is defined as the sampling region*.

For a relatively large time constant ($\Gamma \ll 2$), the operation of the circuit can be understood by looking at the branch currents (the Norton equivalent in Fig. 7). With the large RC-time constant, the resistor can conceptually be moved after the switch (as illustrated in gray) because there is basically no time for the resistor to discharge the capacitor in a cycle. By doing so, the node before the switch has no defined voltage when the switch is opened. In developing an intuitive feeling for the *output* voltage, this can be ignored. We see that the input current is multiplied by the clock and low-pass filtered at the output, identical in operation to a switching mixer. Therefore, *the part of the design space for which* $\Gamma \ll 2$ *is defined as the mixing region*.

Note that the naming of the regions does not reflect the application but merely the similarity in operation, i.e., a sampling region SE kernel can be used as a downconverter.

B. LPTV Analysis

For the LPTV analysis, the timing definitions from Opal and Vlach [16] in Fig. 8 are used, where

$$\sigma_0 = 0 \qquad \sigma_k = \sum_{i=1}^{k} \tau_i, \qquad k = 1, \ldots, K. \tag{20}$$

The switching pattern is periodic about time T_s (having a frequency of $f_s = 1/T_s$) and defines K intervals during which the system has a valid LTI state-space description. The kth interval is defined during time $nT_s + \sigma_k < t < nT_s + \sigma_{k+1}$ (where n is an integer).

The HTFs of the kernels can be calculated by the method based on state-space system modeling as described by Ström and Signell [17]. Several properties make the calculations easier.

1) The polyphase decomposition into single-state kernels reduces all matrix operations into scalar ones.
2) The kernel capacitor voltage is both state and output.
3) Circuit analysis reveals that the state has no discontinuous jumps during the switching moments.

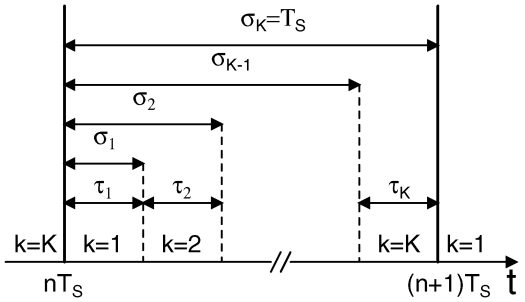

Fig. 8. Timing diagram of the intervals.

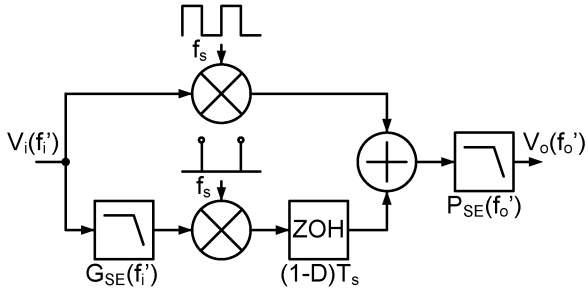

Fig. 9. SE kernel block diagram, equivalent to (28). For harmonic index n, the normalized input frequency is $f_i' = f_o' - n$.

With these simplifications, Appendix A derives a method for calculating the HTFs, using the following:

1) the state-space matrices A_k and B_k for each interval, defined in (67);
2) the frequency-domain response of the output sampled at the switching moments G_k, as defined in (76).

The SE kernel [Fig. 4(a)] has two intervals. Linear analysis reveals that the switch-on interval ($k = 1$) has the state-space description

$$\frac{d}{dt}v_o(t) = -\frac{1}{RC}v_o(t) + \frac{1}{RC}v_i(t), \qquad nT_s \le t < nT_s + \sigma_1 \tag{21}$$

so $A_1 = -(1/RC) \equiv -2\pi f_{rc}$, and $B_1 = (1/RC) \equiv 2\pi f_{rc}$. The switch-off interval ($k = 2$) has the state-space description

$$\frac{d}{dt}v_o(t) = 0, \qquad nT_s + \sigma_1 \le t < (n+1)T_s \tag{22}$$

so $A_2 = 0$, and $B_2 = 0$. The switching-moment transfer functions G_k for the SE kernel are derived in Appendix B.

For the two intervals, (78) is evaluated by inserting A_k, B_k, and G_k

$$\begin{aligned} H_{n,1}(f) &= \frac{f_{rc}}{jf + f_{rc}} \frac{1 - e^{-j2\pi n f_s \tau_1}}{j2\pi n} \\ &\quad - \frac{jf}{jf + f_{rc}} f_s \frac{e^{j2\pi f \tau_2} - 1}{j2\pi f} G_0(f - nf_s) \\ H_{n,2}(f) &= f_s \frac{e^{j2\pi f \tau_2} - 1}{j2\pi f} G_0(f - nf_s). \end{aligned} \tag{23}$$

Summing according to (79) and applying

$$1 - \frac{jf}{jf + f_{rc}} = \frac{f_{rc}}{jf + f_{rc}} \tag{24}$$

give the HTFs, which are a function of the output frequency $f_o = f$. According to (80)

$$\begin{aligned} H_n(f_o) = \frac{f_{rc}}{jf_o + f_{rc}} \Bigg[&\frac{1 - e^{-j2\pi n f_s \tau_1}}{j2\pi n} \\ &+ f_s \frac{e^{j2\pi - f_o \tau_2} - 1}{j2\pi f_o} G_0(f_o - nf_s) \Bigg]. \end{aligned} \tag{25}$$

This expression can be simplified. The duty cycle D is the duration of the first interval relative to the period time

$$D = \frac{\tau_1}{T_s} = \tau_1 f_s \qquad (1 - D) = \frac{\tau_2}{T_s} = \tau_2 f_s. \tag{26}$$

If these expressions are substituted into (25), then all frequencies can be normalized to the switching frequency f_s. The normalized frequencies are defined as

$$f_o' \equiv \frac{f_o}{f_s} \qquad f_{rc}' \equiv \frac{f_{rc}}{f_s}. \tag{27}$$

The HTFs are rewritten in normalized frequencies as

$$\begin{aligned} H_{n,\mathrm{SE}}(f_o') = P_{\mathrm{SE}}(f_o') \Bigg[&\frac{1 - e^{-j2\pi D n}}{j2\pi n} \\ &+ \frac{e^{j2\pi(1-D)f_o'} - 1}{j2\pi f_o'} G_{\mathrm{SE}}(f_o' - n) \Bigg] \end{aligned} \tag{28}$$

where

$$P_{\mathrm{SE}}(f_o') \equiv \frac{1}{1 + j\frac{f_o'}{f_{rc}'}} \tag{29}$$

and in normalized input frequency $f_i' = f_i/f_s = f_o' - n$

$$G_{\mathrm{SE}}(f_i') \equiv G_0(f_i') = \frac{e^{j2\pi D f_i'} - e^{-2\pi D f_{rc}'}}{e^{j2\pi f_i'} - e^{-2\pi D f_{rc}'}} \frac{1}{1 + j\frac{f_i'}{f_{rc}'}}. \tag{30}$$

Equation (28) describes the *exact SE kernel frequency-domain behavior for all duty cycles D and RC bandwidths f_{rc}*. The HTFs are also represented by the block diagram in Fig. 9, which consists of filters G_{SE} and P_{SE}, a zero-order hold, ideal multipliers, and a summing node.

For the DI kernel in Fig. 4(b), the same procedure is used. The DI kernel has four intervals. The first interval ($nT_s \le t < (n + D)T_s$) has duty cycle D with

$$\frac{d}{dt}v_o(t) = -\frac{1}{RC}v_o(t) + \frac{1}{2RC}v_i(t). \tag{31}$$

The second interval ($(n + D)T_s \le t < (n + (1/2))T_s$) ends after half the period time

$$\frac{d}{dt}v_o(t) = 0. \tag{32}$$

In the third interval ($(n+(1/2))T_s \le t < (n+(1/2)+D)T_s$), the negative input is connected

$$\frac{d}{dt}v_o(t) = -\frac{1}{RC}v_o(t) - \frac{1}{2RC}v_i(t). \tag{33}$$

For the final interval ($(n + (1/2) + D)T_s \le t < (n + 1)T_s$)

$$\frac{d}{dt}v_o(t) = 0. \tag{34}$$

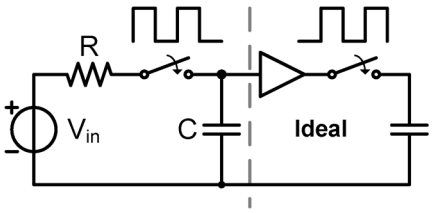

Fig. 10. SE kernel time-discrete schematic.

The calculation of G_k is very similar to the SE-kernel case in Appendix B.

Ultimately, the HTFs for the DI kernel can be derived as

$$H_{n,\mathrm{DI}}(f_o') = P_{\mathrm{DI}}(f_o') \left[\frac{1-e^{-j2\pi Dn}}{j2\pi n} + \frac{e^{j2\pi\left(\frac{1}{2}-D\right)f_o'}-1}{j2\pi f_o'} G_{\mathrm{DI}}(f_o'-n) \right] \tag{35}$$

where

$$P_{\mathrm{DI}}(f_o') \equiv \frac{\left(1-e^{-j2\pi\frac{1}{2}n}\right)}{2} \frac{1}{1+j\frac{f_o'}{f_{rc}'}} \tag{36}$$

$$G_{\mathrm{DI}}(f_i') \equiv -\frac{e^{j2\pi Df_i'}-e^{-2\pi Df_{rc}'}}{e^{j2\pi\frac{1}{2}f_i'}+e^{-2\pi Df_{rc}'}} \frac{1}{1+j\frac{f_i'}{f_{rc}'}}. \tag{37}$$

Equation (35) describes the *exact DI kernel frequency-domain behavior for all duty cycles D and RC bandwidths f_{rc}*. It is very similar to the one derived for the SE kernel. The extra $(1-e^{-j2\pi(1/2)n})/2$ evaluates to zero for all even n and to unity for all odd n.

C. Discrete-Time Output

In sampling systems, the output is the discrete-time voltage held on the capacitor. In such cases, a second switch and a capacitor (presumed ideal) take over the capacitor voltage for further processing, shown schematically in Fig. 10.

The discrete-time transfer function is simply G_{SE}, and the sampled-and-held output is expressed as

$$H_{n,\mathrm{SE,DT}}(f_o') = \frac{e^{j2\pi f_o'}-1}{j2\pi f_o'} \cdot G_{\mathrm{SE}}(f_o'-n). \tag{38}$$

VI. Kernel Sampling and Mixing Region

In this section, the distinction between the kernel sampling and mixing regions, as described in the qualitative analysis in Section V, is further explored. Section VI-A derives simplified expressions for G_{SE}, which are used in Section VI-B to derive approximate HTFs for the two regions. Using these results, Section VI-C derives the output noise PSD and the total output noise power for each region. Section VI-D motivates the choice for the $\Gamma = 2$ borderline between the regions and further discusses the region differences.

The equations are written using the sinc form (93), and some integrals and sums from Appendix C are used.

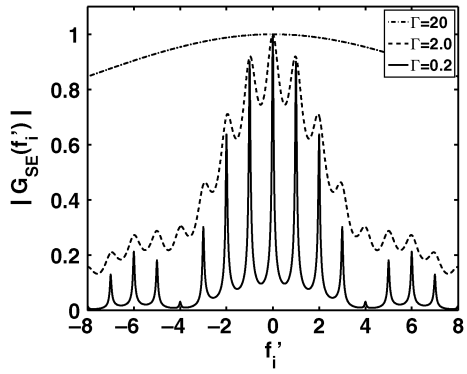

Fig. 11. G_{SE} plotted versus normalized input frequency $f_i' = f_i/f_s$ for several Γ and duty cycle $D = 0.25$.

A. Switching Moments

A plot of the switching-moment transfer function $G_{\mathrm{SE}}(f_i')$ (30) is shown in Fig. 11 for several values of Γ (19). It is clear from the figure that G_{SE} is shaped differently for various Γ and that approximate (and simpler) expressions can be derived.

1) Sampling Region: The sampling region was defined by $\Gamma \gg 2$. The duty cycle is bounded $0 \le D \le 1$, so (30) has to be considered for large values of f_{rc}'

$$G_{\mathrm{SE}}(f_i') \approx e^{-j2\pi f_i'(1-D)} \frac{1}{1+j\frac{f_i'}{f_{rc}'}}, \qquad \Gamma \gg 2. \tag{39}$$

2) Mixing Region: For the mixing region, defined as $\Gamma \ll 2$, the limit of $\Gamma \to 0$ is calculated. In order to get a meaningful limit result, we need to scale f_i' appropriately with Df_{rc}', namely, as $f_i' = aDf_{rc}' - n$ for constant a; otherwise, the limit of the HTFs is zero at noninteger f_i'. The scaling reflects the fact that the peaks around integer f_i' in Fig. 11 become narrower as Df_{rc}' decreases. Rewriting (30) in terms of a

$$G_{\mathrm{SE}}(aDf_{rc}'-n) = \frac{e^{j2\pi D\left(aDf_{rc}'-n\right)}-e^{-2\pi Df_{rc}'}}{e^{-j2\pi n}e^{j2\pi aDf_{rc}'}-e^{-2\pi Df_{rc}'}} \cdot \frac{1}{1+j\frac{aDf_{rc}'-n}{f_{rc}'}}. \tag{40}$$

We first consider the limit of small f_{rc}' at constant D and $n \neq 0$

$$\begin{aligned} &\lim_{f_{rc}'\to 0} G_{\mathrm{SE}}(aDf_{rc}'-n) \\ &= \lim_{f_{rc}'\to 0} \frac{e^{-j2\pi Dn}-e^{-2\pi Df_{rc}'}}{1\cdot e^{j2\pi aDf_{rc}'}-e^{-2\pi Df_{rc}'}} \cdot \frac{1}{1+jaD-j\frac{n}{f_{rc}'}} \\ &= \lim_{f_{rc}'\to 0} \frac{e^{-j2\pi Dn}\cdot 1-1}{(1+j2\pi aDf_{rc}')-(1-2\pi Df_{rc}')+\mathcal{O}\left({f_{rc}'}^2\right)} \cdot \frac{f_{rc}'}{-jn} \\ &= \frac{1}{ja+1}\mathrm{sinc}(Dn)e^{-j\pi Dn}. \end{aligned} \tag{41}$$

Next, a similar calculation gives the limit for small D at constant f_{rc}' and $n \neq 0$

$$\lim_{D\to 0} G_{\mathrm{SE}}(aDf_{rc}'-n) = \frac{1}{ja+1}. \tag{42}$$

Calculations for $n = 0$ yield the same results. Comparing both limits, we can conclude that, for small values of Γ (i.e., either D or f'_{rc} or both are small) and corresponding small values of f'_o, we have

$$G_{\mathrm{SE}}(f'_o - n) \approx \frac{\mathrm{sinc}(Dn)e^{-j\pi Dn}}{1 + j\frac{f'_o}{Df'_{rc}}}, \qquad \Gamma \ll 2. \tag{43}$$

B. HTFs

With the calculated G_{SE}, the complete continuous-time transfer function for the mixing and sampling regions can be derived.

1) Mixing Region: For the mixing region, first, the exact HTFs (28) are put into an alternate form (where $f'_i = f_o - n$)

$$\begin{aligned} H_{n,\mathrm{SE}}(f'_o) = {} & D\frac{1}{1 + j\frac{f'_o}{Df'_{rc}}}\frac{1 - e^{-j2\pi Dn}}{j2\pi Dn} \\ & + (1 - D)\frac{e^{j2\pi(1-D)f'_o} - 1}{j2\pi(1-D)f'_o}G_{\mathrm{SE}}(f'_i) \\ & + (1 - D)\frac{j\frac{f'_o}{f'_{rc}}}{1 + j\frac{f'_o}{f'_{rc}}} \\ & \times \left[\frac{1}{1 + j\frac{f'_o}{Df'_{rc}}}\frac{1 - e^{-j2\pi Dn}}{j2\pi Dn}\right. \\ & \left. - \frac{e^{j2\pi(1-D)f'_o} - 1}{j2\pi(1-D)f'_o}G_{\mathrm{SE}}(f'_i)\right]. \end{aligned} \tag{44}$$

For small f'_o and small Df'_{rc}

$$\frac{e^{j2\pi(1-D)f'_o} - 1}{j2\pi(1-D)f'_o}G_{\mathrm{SE}}(f'_o - n) \approx G_{\mathrm{SE}}(f'_o - n) \tag{45}$$

so that (43) gives

$$\frac{e^{j2\pi(1-D)f'_o} - 1}{j2\pi(1-D)f'_o}G_{\mathrm{SE}}(f'_o - n) \approx \frac{1}{1 + j\frac{f'_o}{Df'_{rc}}}\frac{1 - e^{-j2\pi Dn}}{j2\pi Dn}. \tag{46}$$

Therefore, the bracketed term in (44) vanishes, and the HTFs for the mixing region become

$$H_{n,\mathrm{SE}}(f'_o) \approx \frac{\mathrm{sinc}(Dn)}{1 + j\frac{f'_o}{Df'_{rc}}}e^{-j\pi Dn}, \qquad \Gamma \ll 2. \tag{47}$$

The maximum value of the transfer function depends on the sinc of $D{\cdot}n$. For each frequency shift, low-pass filtering as a function of output frequency occurs.

2) Sampling Region: The substitution of (39) into (28) gives the HTFs for the sampling region as (48), shown at the bottom of the page. From the two terms, part A is the contribution of the track interval when the switch is closed. Part B is the contribution of the hold interval when the switch is opened.

C. Kernel Noise

The noise calculations assume white thermal noise generated by the resistance R with double-sided PSD

$$N_i = 2kTR. \tag{49}$$

Then, the output noise PSD is expressed as (3)

$$N_o(f_o) = 2kTR\sum_{n=-\infty}^{\infty}|H_n(f_o)|^2. \tag{50}$$

The PSD will also be integrated over f_o to find the total noise power P_o

$$P_o = \int_{-\infty}^{\infty}|N_o(f_o)|^2\,df_o. \tag{51}$$

The output noise PSD and the total noise power will be calculated from the approximate HTFs of the mixing (47) and sampling (48) regions.

1) Mixing Region: The HTFs for the mixing region have a factor solely depending on n and a low-pass factor solely depending on f_o. Therefore, we first calculate the PSD for zero output frequency and then multiply by the equivalent noise bandwidth to get the total output noise power. Summing (47) over n for $f_o = 0$ according to (50) and using (97) give

$$N_o(0) = N_i\sum_{n=-\infty}^{\infty}\mathrm{sinc}^2(Dn) = 2kTR\frac{1}{D}, \qquad \Gamma \ll 2. \tag{52}$$

Using (95), the equivalent noise bandwidth B_n is

$$B_n = \int_{-\infty}^{\infty}\left|\frac{1}{1 + j\frac{f_o}{Df_{rc}}}\right|^2 df_o = \frac{D}{2RC} \tag{53}$$

so that the total noise power is equal to that of an LTI RC network

$$P_o = N_o(0)\cdot B_n = \frac{kT}{C}. \tag{54}$$

$$H_{n,\mathrm{SE}}(f'_o) \approx \frac{1}{1 + j\frac{f'_o}{f_{rc'}}}\left[\underbrace{D\,\mathrm{sinc}(Dn)e^{-j\pi Dn}}_{\text{Part A}} + \underbrace{(1 - D)\frac{\mathrm{sinc}\left((1-D)f'_o\right)}{1 + j\frac{f'_o - n}{f_{rc'}}}e^{-j\pi(1-D)f'_o}e^{-j2\pi Dn}}_{\text{Part B}}\right], \qquad \Gamma \gg 2 \tag{48}$$

2) Sampling Region: The same strategy can be used for the sampling region HTFs (48). For parts A and B in (48)

$$|A+B|^2 = |A|^2 + AB^* + A^*B + |B|^2 \tag{55}$$

where * denotes the complex conjugate. Therefore, the sum over n in (50) for zero output frequency ($f_i' = -n$) is expressed as (56), shown at the bottom of the page. Using (96)–(98), this evaluates to

$$N_o(0) \approx 2kT\left[\underbrace{DR}_{AA^*} + \underbrace{\frac{(1-D)^2}{2f_sC}}_{BB^*} + \underbrace{2(1-D)R}_{AB^*+A^*B}\right], \qquad \Gamma \gg 2. \tag{57}$$

Note that, for $\Gamma \gg 2$, the BB^* term, contributed by the hold interval, is dominant.

Finding the equivalent noise bandwidths of these terms is complicated because of the low-pass input filter in (48). The calculations are made easier by assuming the following.

1) Part A is dominated in bandwidth by $(1/1 + j(f_o/f_{rc}))$.
2) Part B is dominated in bandwidth by $\mathrm{sinc}((1-D)f_o')$.
3) The integrated cross terms AB^* and A^*B are zero.

Parts A and B do not overlap in the time domain; therefore, the integrated cross-power spectrum must be zero according to Parseval's theorem

$$\int_{-\infty}^{\infty} A(f)B^*(f)\,df = \int_{-\infty}^{\infty} a(t)b^*(t)\,dt = 0. \tag{58}$$

Using (94) and (95), the noise equivalent bandwidths are

$$B_{n,AA^*} = \int_{-\infty}^{\infty}\left|\frac{1}{1+j\frac{f_o}{f_{rc}}}\right|^2 df_o = \frac{1}{2RC} \tag{59}$$

$$B_{n,BB^*} = \int_{-\infty}^{\infty}\mathrm{sinc}^2\left((1-D)\frac{f_o}{f_s}\right)df_o = \frac{f_s}{1-D}. \tag{60}$$

Therefore, we see that the track interval (part A) has a lower low-frequency PSD but a much higher noise bandwidth than the hold interval (part B). If we calculate the total noise power

$$\begin{aligned} P_o &= N_{o,AA^*}(0)\cdot B_{n,AA^*} + N_{o,BB^*}(0)\cdot B_{n,BB^*} \\ &= D\frac{kT}{C} + (1-D)\frac{kT}{C} = \frac{kT}{C} \end{aligned} \tag{61}$$

we find that the total integrated noise is the well-known kT/C for sampled-data systems. It is distributed proportionally to the interval length over the track-and-hold interval.

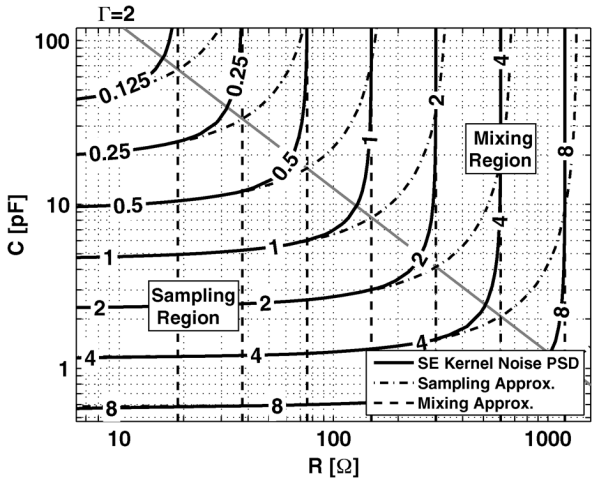

Fig. 12. Contour plot of the SE kernel noise PSD ($f_o = 0\,\mathrm{Hz}$, $f_s = 100\,\mathrm{MHz}$, and $D = 25\%$) [$10^{-17}\,\mathrm{V}^2/\mathrm{Hz}$] calculated by substituting HTFs (28) into (3), with sampling (57) and mixing (52) region approximation.

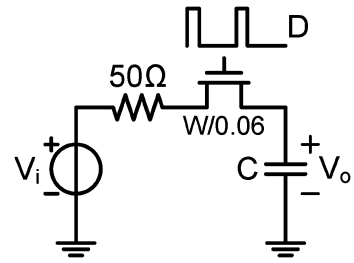

Fig. 13. Application example, SE kernel.

D. Region Comparison and Boundary

Fig. 12 shows a contour of the mixing region PSD (52) and sampling region PSD (57) in dashed lines and the 10 000 term evaluation of the exact PSD [(3) and (28)] in solid lines. In their respective regions, the approximations are fairly good and show an interesting property.

1) For the mixing region, the noise PSD is determined mostly by the resistance R.
2) For the sampling region, the noise PSD is determined mostly by the capacitance C.

When dimensioning a circuit for noise, this difference between the two regions is crucial. Furthermore, we can see that (52) and (57) are equal for $\Gamma = 2$, i.e., the dashed lines intersect on the gray $\Gamma = 2$ line. This motivates our choice for the border between the two regions.

It is not surprising that the total integrated noise power is equal to kT/C for *both* regions. Usually, the integrated noise is obtained with a time-domain approach [12], and it is comforting that our frequency-domain analysis produces the same results.

For a given switching frequency f_s, duty cycle D, and RC bandwidth f_{rc}, the kernel HTFs are a function of the harmonic

$$N_o(0) = N_i\sum_{n=-\infty}^{\infty}\left[\underbrace{D^2\,\mathrm{sinc}^2(Dn)}_{AA^*} + \underbrace{(1-D)^2\left|\frac{1}{1-j\frac{n}{f_{rc}'}}\right|^2}_{BB^*} + \underbrace{(1-D)\frac{D\,\mathrm{sinc}(Dn)}{1+j\frac{n}{f_{rc}'}}e^{j\pi Dn}}_{AB^*} + \underbrace{(1-D)\frac{D\,\mathrm{sinc}(Dn)}{1-j\frac{n}{f_{rc}'}}e^{-j\pi Dn}}_{A^*B}\right] \tag{56}$$

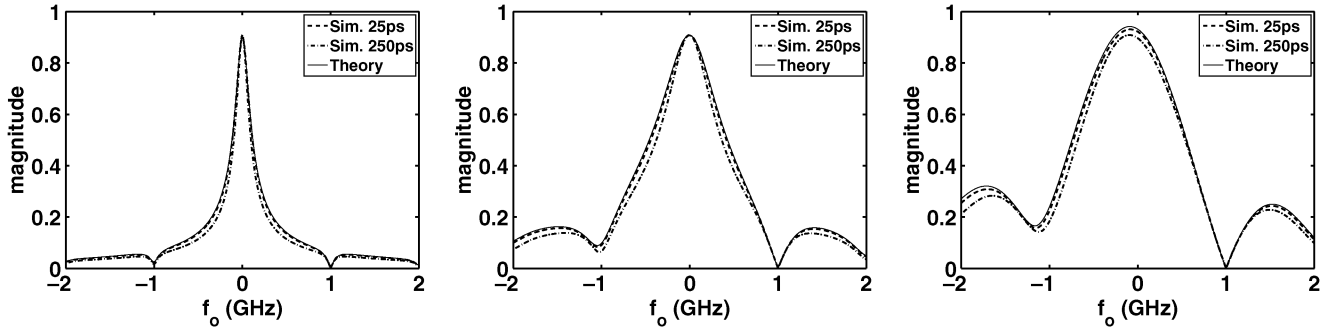

Fig. 14. SE kernel simulated and calculated downconversion HTF ($n = -1$) for 25% duty cycle and several values of Γ. An ideal square-wave clock of 1 GHz and fixed $R_{sw} = 50\ \Omega$ is used for theoretical derivations, whereas finite rise and fall times of 25 and 250 ps are used in the simulations. (a) Mixing region, $\Gamma = 1/2$. (b) Borderline, $\Gamma = 2$. (c) Sampling region, $\Gamma = 8$.

index n and the output frequency f_o. We now investigate the dependence of the approximate HTFs on these two arguments. The mixing region HTFs (47) depend upon n and f_o such that

$$|H_{n,\mathrm{SE}}(f_o')| \propto |\mathrm{sinc}(Dn)|, \qquad \Gamma \ll 2 \tag{62}$$

$$|H_{n,\mathrm{SE}}(f_o')| \propto \frac{1}{\left|1 + j\frac{f_o'}{Df_{rc}'}\right|}, \qquad \Gamma \ll 2 \tag{63}$$

a low-pass filter as a function of *output frequency* f_o and a sinc filter as a function of *frequency shift* nf_s. Similarly, the sampling region HTFs (48) for low duty cycle D depend on n and f_o like

$$|H_{n,\mathrm{SE}}(f_o')| \propto \frac{1}{\left|1 + j\frac{n}{f_{rc}'}\right|}, \qquad \Gamma \gg 2 \tag{64}$$

$$|H_{n,\mathrm{SE}}(f_o')| \propto |\mathrm{sinc}((1-D)f_o')|, \qquad \Gamma \gg 2 \tag{65}$$

a low-pass filter as a function of *frequency shift* nf_s and a sinc filter as a function of *output frequency* f_o. We conclude that the finite RC bandwidth results in filtering of *output frequencies* for the mixing region and filtering of *frequency shifts* for the sampling region.

As a side note, in order to retain the same fractional bandwidth and output noise PSD, for both regions, a scaling of the switching frequency f_s requires only an inverse scaling of the capacitance C.

Thus, we see that the analysis renders interesting insights that assist circuit design. We exemplify this further in the next section.

VII. Application Example

In this section, the application of the derived equations is illustrated by an example downconversion mixer design. Circuit simulations are performed with 65-nm-minimum-length CMOS switches (PSP MOS model [18]) in Cadence, using the periodic steady-state analysis. Suppose that the goal is to dimension a direct-downconversion mixer ($w = -1$) with the following properties:

1) 50-Ω source impedance R_s;
2) 1-GHz-LO-frequency f_s full-swing square-wave clock;
3) 100-MHz baseband bandwidth;
4) SE input;
5) I/Q image rejection.

With an SE input, the choice for an SE kernel, shown in Fig. 13, is obvious. For a given total series resistance $R = 50\ \Omega + R_{\mathrm{on}}$, capacitance C, and duty cycle D, (28) gives the exact HTFs. Arbitrarily beginning with a duty cycle of 25% and a switch-on resistance (set by the NMOS width W) equal to the source impedance, Fig. 14 shows the simulated and calculated HTF magnitudes for $n = -1$ and several values of Γ. In each plot, two simulated curves are included, with 25- and 250-ps clock rise/fall time, respectively. In all cases, the derived equations give an accurate model for the simulated results, even for an almost triangle clock wave.

For the dimensioning of the SE kernel, the derived results in Section VI are used to choose between the mixing and the sampling region. The operating region of the kernel depends on Γ, defined in (19). From the mixing region ($\Gamma \ll 2$) approximate HTFs (47), the following properties were derived:

1) antialias sinc filter, with -3-dB cutoff roughly at $n = 1/(2D)$ (62);
2) baseband low-pass filter with -3-dB cutoff at $f_o = D \cdot f_{rc}$ (63);
3) output noise PSD scaling with resistance (52).

From the sampling region ($\Gamma \gg 2$) approximate HTFs (48), the following properties were derived:

1) antialias low-pass filter with -3-dB cutoff at $n = f_{rc}/f_s$ (64);
2) baseband sinc filter, with -3-dB cutoff roughly at $f_o = f_s/2$ (65);
3) output noise PSD scaling mostly with capacitance (57).

Because of the better suppression of higher frequency shifts nf_s and the ease of setting a baseband bandwidth, the mixing region is chosen. The required capacitance to set the correct bandwidth is (18)

$$C = \frac{D}{2\pi(50\ \Omega + R_{\mathrm{on}}) \cdot 100\ \mathrm{MHz}}. \tag{66}$$

This also ensures that $\Gamma < 2$ so that the kernel operates in the mixing region.

With the HTFs from (28) inserted into (8), the kernel NF is shown in Fig. 15. Clearly, lower switch-on resistances give better NFs (mixing region in Fig. 12), and we choose $R_{\mathrm{on}} = 5\ \Omega$.

In Section IV-A, it was concluded that a minimum of three polyphase paths are needed for image rejection. However, I/Q outputs are preferred for demodulation, so a four-path system was chosen ($L = 4$). The resulting mixer circuit is shown in Fig. 16. Fig. 15 also shows the NF versus duty cycle, showing an optimum around $D = 40\%$. As the maximum duty cycle avoiding overlap is 25%, this is the choice.

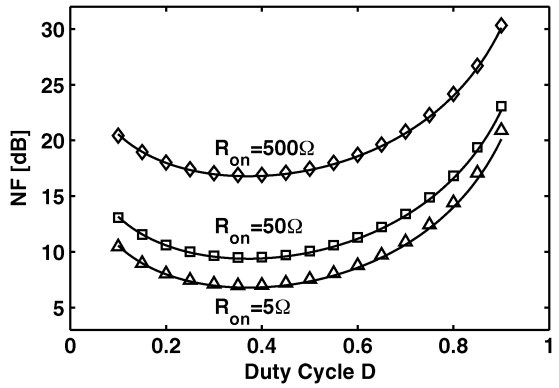

Fig. 15. SE kernel (markers) simulated and (lines) calculated NF for several $R_{\rm on}$, swept over duty cycle ($\Gamma < 2$).

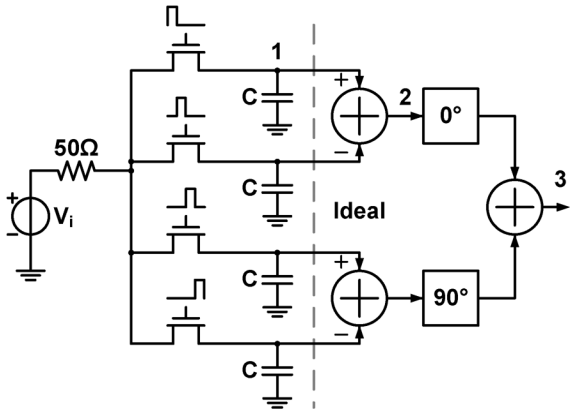

Fig. 16. Application example, complete mixer.

With the dimensioning finished, a simulation of the voltages on the mixer nodes in Fig. 17 confirms the cancellation of the image, and all frequency shifts with even n. Due to the polyphase combining, a 6-dB improvement in NF and a 12-dB improvement in conversion gain are observed, as predicted by (13) and (17), respectively.

To illustrate the diversity of our analysis, calculations of conversion gain and NF of published passive mixers were compared with the reported numbers in Table I.

VIII. Conclusion

It has been shown that a group of passive mixers and samplers can be described by multipath polyphase systems of SE or DI switched-series-RC kernels. The identification of kernels combined in a polyphase manner greatly simplified the calculation of the HTFs and provides helpful design insights. Unlike the equations in literature, the derived expressions are valid for the complete design space spanned by the duty cycle, RC-time constant, and output frequency. The derived conversion gain, output noise, and NF equations clearly show two distinct operating regions, defined as the mixing and sampling regions. The borderline between the two regions is determined by the noise behavior and corresponds to a ratio between the switching frequency and RC bandwidth equal to π times the duty cycle. From the exact HTFs, easier-to-use approximate expressions were derived for each region. It was shown that the output noise PSD depends mostly on the resistance for the mixing region and on the capacitance for the sampling region. Moreover, it was concluded that the finite RC bandwidth results in a baseband low-pass filter for the mixing region and a built-in "antialias" filter for the sampling region. Our analysis has been supported by circuit simulations and performance calculations of published mixers.

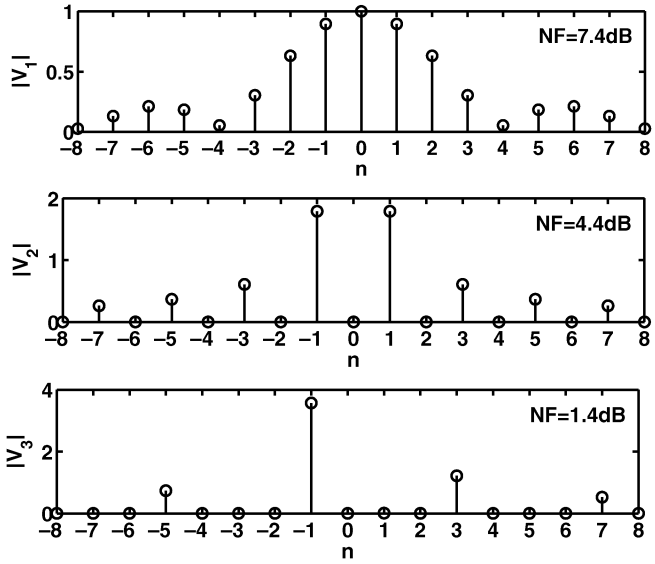

Fig. 17. Magnitude of the simulated HTFs of the voltage on nodes 1, 2, and 3 in Fig. 16 for $f_o = 0$ Hz.

Appendix A
LPTV Calculation Method

Ström and Signell [17] made three observations. First, the response in an interval depends only on the input stimulus and initial interval conditions

$$\frac{d}{dt}v_o(t) = A_k v_o(t) + B_k v_i(t), \quad nT_s + \sigma_{k-1} \le t < nT_s + \sigma_k \tag{67}$$

where $v_i(t)$ is the input voltage, $v_o(t)$ is the output voltage, and A_k and B_k are the state-space parameters defining this first-order system. Second, if $v_{o,k}(t)$ is defined as being equal to zero outside and equal to the output voltage inside the kth interval (Fig. 18)

$$v_{o,k}(t) = v_o(t) \cdot w_k(t) \tag{68}$$

$$w_k(t) = \begin{cases} 1, & nT_s + \sigma_{k-1} \le t < nT_s + \sigma_k \\ 0, & \text{elsewhere} \end{cases} \tag{69}$$

then the output is the sum of all $v_{o,k}(t)$

$$v_o(t) = \sum_{k=1}^{K} v_{o,k}(t). \tag{70}$$

Finally, the state-space response (67) can be made zero outside the interval by disconnecting the input source and subtracting the final conditions at the interval end [17, eq. (7)]

$$\begin{aligned} \frac{d}{dt}v_{o,k}(t) = {} & A_k v_{o,k}(t) + B_k v_{i,k}(t) \\ & + \sum_{n=-\infty}^{\infty} \left[v_o(t)\delta(t - nT_s - \sigma_{k-1}) \right. \\ & \left. - v_o(t)\delta(t - nT_s - \sigma_k) \right], \\ & -\infty < t < \infty \end{aligned} \tag{71}$$

where

$$v_{i,k}(t) = v_i(t) \cdot w_k(t) \tag{72}$$

and $\delta(t)$ is the Dirac delta function.

TABLE I
PUBLISHED PASSIVE MIXERS

Year Name	f_s	Kernel	Duty Cycle D	Γ[1]	L [2]	w [3]	$\frac{R_{on}}{R_s}$	Reported Gain [dB]	Reported NF [dB]	Calculated Gain [dB] [7]	Calculated NF [dB] [8]
1997 Shahani [9]	1.61GHz	DI	50%	< 2	2	-1	n/a	-3.6 [5]	10 [5]	-3.9	n/a
2005 Zhou [19]	5.1-5.4GHz	SE	50%	< 2	2	-1	20	2.1 [6]	17 [4,6]	2.1	17.1
2009 Soer [1]	0.2-2.0GHz	DI	25%	< 0.2	4	-1	$\frac{1}{10}$	5.1 [6]	1.8 [6]	5.1	1.9
1993 Chan [20]	50MHz	SE	50%	200	2	-19	3	-6 [5]	18 [5]	-6.3 [9]	19.3 [9]
1997 Parssinen [11]	500MHz	SE	18%	> 2	1	-4	n/a	-2 [6]	23 [5]	-2.1	n/a

[1] < 2: Mixing Region, >2: Sampling Region
[2] Number of polyphase paths
[3] Harmonic index of desired frequency conversion
[4] 14 dB DSB noise figure reported, SSB noise figure is 17 dB
[5] Measured in publication
[6] Estimated / derived in publication
[7] Gain as defined in (4), with HTFs (28) for the SE kernel and (35) for the DI kernel, including the gain of polyphase combining (13).
[8] NF as defined in (8), with HTFs (28) for the SE kernel and (35) for the DI kernel, including the contribution of polyphase combining (17).
[9] Single-ended to differential conversion introduces an extra 1/2 gain factor and a 1 GHz input bandwidth limits the contributions in (8) to $n = -20 \ldots 20$.

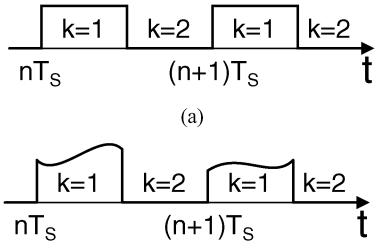

Fig. 18. Example of (a) $w_1(t)$ and (b) $v_{o,1}(t)$.

Because (71) is valid for all t, the Fourier transform [denoted by $\mathcal{F}()$] can be used. The Fourier transforms of (71) and (70) are

$$\begin{aligned}(j2\pi f - A_k)V_{o,k}(f) &= B_k \cdot \mathcal{F}\left(v_i(t) \cdot w_k(t)\right) \\ &\quad + \sum_{n=-\infty}^{\infty} \left[\mathcal{F}\left(v_o(t) \cdot \delta(t - nT_s - \sigma_{k-1})\right)\right. \\ &\qquad \left. - \mathcal{F}\left(v_o(t) \cdot \delta(t - nT_s - \sigma_k)\right)\right] \quad (73)\end{aligned}$$

$$V_o(f) = \sum_{k=1}^{K} V_{o,k}(f). \quad (74)$$

The multiplication of $w_k(t)$ and $v_i(t)$ becomes a convolution in the frequency domain resulting in [21, eq. (6.20) + (5.13)]

$$\mathcal{F}\left(v_i(t) \cdot w_k(t)\right) = \sum_{n=-\infty}^{\infty} \frac{1 - e^{-j2\pi n f_s \tau_k}}{j2\pi n} e^{-j2\pi n f_s \sigma_{k-1}} V_i(f - nf_s). \quad (75)$$

To obtain a closed-form expression for the transfer function, we want to express the sampled output voltage terms in (73) as a function of the input voltage. Suppose that there is a function $G_k(f)$ such that the output voltage at switching moment $t = nT_s + \sigma_k$ can be expressed as

$$\sum_{n=-\infty}^{\infty} \mathcal{F}\left(v_o(t)\delta(t - nT_s - \sigma_k)\right) = \sum_{n=-\infty}^{\infty} \left[G_k(f) \cdot \mathcal{F}\left(v_i(t)\right)\right] * \delta(f - nf_s) \cdot f_s e^{-j2\pi n f_s \sigma_k} \quad (76)$$

where the * operator is the convolution integral [21, eq. (3.18)]. Working out the Fourier transform [21, eq. (12.7) + (5.13)]

$$\sum_{n=-\infty}^{\infty} \mathcal{F}\left(v_o(t)\delta(t - nT_s - \sigma_k)\right) = \sum_{n=-\infty}^{\infty} G_k(f - nf_s) \cdot f_s e^{-j2\pi n f_s \sigma_k} V_i(f - nf_s). \quad (77)$$

We will show that $G_k(f)$ does exist for the SE and DI kernels.

After filling in the transformed terms, (73) becomes

$$\begin{aligned}V_{o,k}(f) &= \sum_{n=-\infty}^{\infty} H_{n,k}(f) V_i(f - nf_s) \\ H_{n,k}(f) &= \frac{1}{j2\pi f - A_k}\left[B_k \frac{1 - e^{-j2\pi n f_s \tau_k}}{j2\pi n} e^{-j2\pi n f_s \sigma_{k-1}}\right. \\ &\quad + f_s G_{k-1}(f - nf_s) e^{-j2\pi n f_s \sigma_{k-1}} \\ &\quad \left. - f_s G_k(f - nf_s) e^{-j2\pi n f_s \sigma_k}\right]. \quad (78)\end{aligned}$$

According to (74), the total HTFs are then

$$H_n(f) = \sum_{k=1}^{K} H_{n,k}(f). \quad (79)$$

The substitution of (78) into (79) is in the form of the HTF definition (1) if the following notation is introduced:

$$f_o = f \qquad f_i = f - nf_s. \quad (80)$$

We see that G_k must have the input frequency f_i as argument.

APPENDIX B
SE KERNEL G_k

In this Appendix, the switching-moment transfer functions $G_k(f_i)$ are determined for the SE kernel in Fig. 4(a).

During an interval, the LTI system response includes a zero-input term and a zero-initial-value term [21, eq. (8.29) + eq. (8.41)]

$$\begin{aligned} v_{o,k}(t) &= \phi_k(t-t_0)v_{o,k}(t_0) + B_k \int_{t_0}^{t} \phi_k(t-\tau)v_i(\tau)\,d\tau \\ \phi_k(t) &= e^{A_k t}. \end{aligned} \tag{81}$$

For the sinusoidal input ($v_i(t) = e^{j2\pi ft}$), the solution can be calculated directly. During interval 1

$$\begin{aligned} v_{o,1}(t) = e^{-2\pi f_{rc}(t-t_0)}v_{o,1}(t_0) + \frac{1}{1+j\frac{f}{f_{rc}}} \\ \times \left[e^{j2\pi f(t-t_0)} - e^{-2\pi f_{rc}(t-t_0)}\right] e^{j2\pi f t_0} \end{aligned} \tag{82}$$

and during interval 2

$$v_{o,2}(t) = v_{o,2}(t_0). \tag{83}$$

Filling in $t_0 = nT_s$ and $t = nT_s + \sigma_1$ into (82) gives the output voltage at the interval end $v_{o,1}(nT_s+\sigma_1)$ given the input and the initial value $v_{o,1}(nT_s)$. Since the output voltage is continuous, the initial value of an interval is equal to the final value of the previous interval

$$\begin{aligned} v_{o,2}(nT_s+\sigma_1) &= \lim_{t'\uparrow\sigma_1} v_{o,1}(nT_s+t') \\ v_{o,1}\left((n+1)T_s\right) &= \lim_{t'\uparrow\sigma_2} v_{o,2}(nT_s+t'). \end{aligned} \tag{84}$$

Furthermore, (83) gives

$$v_{o,2}(nT_s+\sigma_1) = \lim_{t'\uparrow\sigma_2} v_{o,2}(nT_s+t'). \tag{85}$$

By chaining these expressions, the output voltage after a full cycle can be expressed as

$$\begin{aligned} v_o\left((n+1)T_s\right) = e^{-2\pi f_{rc}\tau_1}v_o(nT_s) + \frac{1}{1+j\frac{f}{f_{rc}}} \\ \times \left[e^{j2\pi f\tau_1} - e^{-2\pi f_{rc}\tau_1}\right] e^{j2\pi f n T_s}. \end{aligned} \tag{86}$$

This result can be viewed as a difference equation with a solution that consists of a steady-state and a transient response. For a frequency-domain description, the transient response can be discarded. With the z transform, it can be calculated that a difference equation of the form

$$v_o\left((n+1)T_s\right) = \alpha \cdot v_o(nT_s) + \beta \cdot e^{j2\pi f n T_s} \tag{87}$$

has the steady-state solution [21, eq. (13.32)]

$$v_o(nT_s) = \frac{\beta}{e^{j2\pi f T_s} - \alpha} \cdot e^{j2\pi f n T_s}. \tag{88}$$

Applying (88) into (86) gives

$$v_o(nT_s) = \left[\frac{e^{j2\pi f\tau_1} - e^{-2\pi f_{rc}\tau_1}}{e^{j2\pi f T_s} - e^{-2\pi f_{rc}\tau_1}} \frac{1}{1+j\frac{f}{f_{rc}}}\right] e^{j2\pi f n T_s} \tag{89}$$

where the term between brackets is defined as $G_0(f)$. We will now show that this is indeed G_0 as defined in (76).

Equation (89) is still in the discrete-time domain and gives the output voltage sampled at the switching moments. By inserting delta impulse functions, (89) is brought into the continuous-time domain

$$\sum_{n=-\infty}^{\infty} v_o(t)\delta(t-nT_s) = \sum_{n=-\infty}^{\infty} G_0(f)\cdot e^{j2\pi ft}\delta(t-nT_s). \tag{90}$$

The aforementioned equation gives the output at the switching moments for a single input sinusoid, represented by $e^{j2\pi ft}$. After replacing $e^{j2\pi ft}$ by the more generic notation $v_i(t)$, we can take the Fourier transform of (90), resulting in

$$\begin{aligned} \sum_{n=-\infty}^{\infty} \mathcal{F}\left(v_o(t)\delta(t-nT_s)\right) \\ = \sum_{n=-\infty}^{\infty} \left[G_0(f)\cdot\mathcal{F}\left(v_i(t)\right)\right] * \delta(f-nf_s)\cdot f_s. \end{aligned} \tag{91}$$

This was derived for $v_i(t)$ being a single sinusoidal input, but because the system is linear, it actually holds for any input signal $v_i(t)$.

Equation (91) corresponds to the definition of G_0 in (76). The same can be done for $v_o(nT_s+\sigma_1)$ and $v_o(nT_s+\sigma_2)$ to find

$$\begin{aligned} G_1(f) &= G_0(f)e^{j2\pi f\tau_2} \\ G_2(f) &= G_0(f). \end{aligned} \tag{92}$$

Appendix C
Integrals and Sums

In this Appendix, the parameters a and b are real numbers. The sinc function is defined as

$$\begin{aligned} \operatorname{sinc}(x) &\equiv \frac{\sin \pi x}{\pi x} = \frac{e^{j\pi x} - e^{-j\pi x}}{j2\pi x} \\ \operatorname{sinc}(0) &= 1 \qquad \Im\left(\operatorname{sinc}(x)\right) = 0. \end{aligned} \tag{93}$$

The integrals using [22, 3.821 9.] and [22, 3.112 2.] are

$$\int_{-\infty}^{\infty} \left|\frac{1-e^{-j2\pi ax}}{j2\pi x}\right|^2 dx = \frac{2}{\pi^2}\int_{0}^{\infty} \frac{\sin^2(\pi ax)}{x^2}\,dx = a \tag{94}$$

$$\int_{-\infty}^{\infty} \left|\frac{1}{1+jbx}\right|^2 dx = \int_{-\infty}^{\infty} \frac{1}{(1+jbx)(1-jbx)}\,dx = \frac{\pi}{b}. \tag{95}$$

The sums using [22, 1.217 1.], [22, 0.233], and [22, 1.443 3.] are

$$\begin{aligned} \sum_{n=-\infty}^{\infty} \left|\frac{1}{1-jbn}\right|^2 = 1 + 2\sum_{n=1}^{\infty} \frac{1}{1+b^2n^2} = \frac{\frac{\pi}{b}}{\tanh\left(\frac{\pi}{b}\right)} \\ \approx \frac{\pi}{b}, \qquad 0 < b \ll 1 \end{aligned} \tag{96}$$

$$\sum_{n=-\infty}^{\infty}\left|\frac{1-e^{-j2\pi an}}{j2\pi n}\right|^2 = a^2 + 2\sum_{n=1}^{\infty}\frac{\sin^2\pi an}{\pi^2 n^2}$$
$$= a^2 + \frac{1}{\pi^2}\left[\sum_{n=1}^{\infty}\frac{1}{n^2} - \sum_{n=1}^{\infty}\frac{\cos 2\pi an}{n^2}\right]$$
$$= a. \qquad (97)$$

The sum using [22, 1.441 1.], [22, 1.217 1.], [22, 1.445 2.], and [22, 1.445 1.] is

$$\sum_{n=-\infty}^{\infty}\frac{e^{j2\pi an}-1}{j2\pi n(1+jbn)}$$
$$= \sum_{n=-\infty}^{\infty}\frac{(e^{j2\pi an}-1)(1+jbn-jbn)}{j2\pi n(1+jbn)}$$
$$= \sum_{n=-\infty}^{\infty}\frac{e^{j2\pi an}-1}{j2\pi n} - b\sum_{n=-\infty}^{\infty}\frac{e^{j2\pi an}-1}{2\pi(1+jbn)}$$
$$= a + 2\sum_{n=1}^{\infty}\frac{\sin(2\pi an)}{2\pi n} + \sum_{n=-\infty}^{\infty}\frac{b}{2\pi(1+b^2n^2)}$$
$$- \sum_{n=-\infty}^{\infty}\frac{b\cos(2\pi an)}{2\pi(1+b^2n^2)} - \sum_{n=-\infty}^{\infty}\frac{b^2 n\sin(2\pi an)}{2\pi(1+b^2n^2)}$$
$$= \frac{1}{2} + \frac{1}{2}\cdot\frac{1+e^{-2\pi b^{-1}}}{1-e^{-2\pi b^{-1}}} - \frac{e^{-2\pi ab^{-1}}}{1-e^{-2\pi b^{-1}}}, \qquad 0<a<1$$
$$\approx 1, \qquad b\to 0. \qquad (98)$$

ACKNOWLEDGMENT

The authors would like to thank Z. Ru and A. Ghaffari for the many discussions.

REFERENCES

[1] M. C. M. Soer, E. A. M. Klumperink, Z. Ru, F. E. van Vliet, and B. Nauta, "A 0.2-to-2.0 GHz 65 nm CMOS receiver without LNA achieving >11 dBm IIP3 and <6.5 dB NF," in *Proc. IEEE ISSCC Dig. Tech. Papers*, 2009, vol. 52, pp. 222–223.

[2] X. He, J. van Sinderen, and R. Rutten, "A 45 nm WCDMA transmitter using direct quadrature voltage modulator with high oversampling digital front-end," in *Proc. IEEE ISSCC Dig. Tech. Papers*, 2010, vol. 53, pp. 62–63.

[3] Z. Ru, E. Klumperink, and B. Nauta, "A discrete-time mixing receiver architecture with wideband harmonic rejection," in *Proc. IEEE ISSCC Dig. Tech. Papers*, 2008, vol. 51, pp. 322–323.

[4] C. Andrews and A. Molnar, "A passive-mixer-first receiver with baseband-controlled RF impedance matching, <6 dB NF, and > 27 dBm wideband IIP3," in *Proc. IEEE ISSCC Dig. Tech. Papers*, 2010, vol. 53, pp. 46–47.

[5] S. Chehrazi, A. Mirzaei, and A. Abidi, "Noise in current-commutating passive FET mixers," *IEEE Trans. Circuits Syst. I, Reg. Papers*, vol. 57, no. 2, pp. 332–344, Feb. 2010.

[6] T. Sowlati, B. Agarwal, J. Cho, T. Obkircher, M. El Said, J. Vasa, B. Ramachandran, M. Kahrizi, E. Dagher, W.-H. Chen, M. Vadkerti, G. Taskov, U. Seckin, H. Firouzkouhi, B. Saeidi, H. Akyol, Y. Choi, A. Mahjoob, S. D'Souza, C.-Y. Hsieh, D. Guss, D. Shum, D. Badillo, I. Ron, D. Ching, F. Shi, Y. He, J. Komaili, A. Loke, R. Pullela, E. Pehlivanoglu, H. Zarei, S. Tadjpour, D. Agahi, D. Rozenblit, W. Domino, G. Williams, N. Damavandi, S. Wloczysiak, S. Rajendra, A. Paff, and T. Valencia, "Single-chip multiband WCDMA/HSDPA/HSUPA/EGPRS transceiver with diversity receiver and 3G DigRF interface without SAW filters in transmitter/3G receiver paths," in *Proc. IEEE ISSCC Dig. Tech. Papers*, 2009, vol. 52, pp. 116–117.

[7] Z. Ru, E. Klumperink, G. Wienk, and B. Nauta, "A software-defined radio receiver architecture robust to out-of-band interference," in *Proc. IEEE ISSCC Dig. Tech. Papers*, 2008, vol. 52, pp. 232–233.

[8] G. Xu and J. Yuan, "A low-voltage high-speed sampling technique," in *Proc. IEEE Int. Conf. ASIC*, 2001, pp. 228–231.

[9] A. R. Shahani, D. K. Shaeffer, and T. H. Lee, "A 12-mW wide dynamic range CMOS front-end for a portable GPS receiver," *IEEE J. Solid-State Circuits*, vol. 32, no. 12, pp. 2061–2070, Dec. 1997.

[10] B. Leung, *VLSI for Wireless Communication*. Englewood Cliffs, NJ: Prentice-Hall, 2002.

[11] A. Parssinen, R. Magoon, S. I. Long, and V. Porra, "A 2-GHz subharmonic sampler for signal downconversion," *IEEE Trans. Microw. Theory Tech.*, vol. 45, no. 12, pp. 2344–2351, Dec. 1997.

[12] R. Gregorian and G. Temes, *Analog MOS Integrated Circuits for Signal Processing*. New York: Wiley, 1986.

[13] D. Tayloe, "Product detector and method therefor," U.S. Patent 6 230 000, May 8, 2001.

[14] B. W. Cook, A. Berny, A. Molnar, S. Lanzisera, and K. S. J. Pister, "Low-power 2.4-GHz transceiver with passive RX front-end and 400-mV supply," *IEEE J. Solid-State Circuits*, vol. 41, no. 12, pp. 2757–2766, Dec. 2006.

[15] M. Liou and Y. Kuo, "Exact analysis of switched capacitor circuits with arbitrary inputs," *IEEE Trans. Circuits Syst.*, vol. CAS-26, no. 4, pp. 213–223, Apr. 1979.

[16] A. Opal and J. Vlach, "Analysis and sensitivity of periodically switched linear networks," *IEEE Trans. Circuits Syst.*, vol. 36, no. 4, pp. 522–532, Apr. 1989.

[17] T. Ström and S. Signell, "Analysis of periodically switched linear circuits," *IEEE Trans. Circuits Syst.*, vol. CAS-24, no. 10, pp. 531–541, Oct. 1977.

[18] G. Gildenblat, X. Lin, W. wu, H. Wang, A. Jha, R. van Langevelde, G. Smit, A. Scholten, and D. Klaassen, "PSP: An advanced surface-potential-based MOSFET model for circuit simulation," *IEEE Trans. Electron Devices*, vol. 53, no. 9, pp. 1979–1993, Sep. 2006.

[19] S. Zhou and M. F. Chang, "A CMOS passive mixer with low flicker noise for low-power direct-conversion receiver," *IEEE J. Solid-State Circuits*, vol. 40, no. 5, pp. 1084–1093, May 2005.

[20] P. Y. Chan, A. Rofougaran, K. A. Ahmed, and A. A. Abidi, "A highly linear 1-GHz CMOS downconversion mixer," in *Proc. Eur. Solid State Circuits Conf.*, 1993, pp. 210–213.

[21] C. L. Phillips and J. M. Parr, *Signals, Systems and Transforms*. Englewood Cliffs, NJ: Prentice-Hall, 1995.

[22] I. Gradshteyn and I. Ryzhik, *Table of Integrals, Series, and Products*, A. Jeffrey, Ed. New York: Academic, 1994

.

Michiel C. M. Soer (S'09) was born in Schoonhoven, The Netherlands, in 1984. He received the M.Sc. degree (*cum laude*) in electrical engineering from the University of Twente, Enschede, The Netherlands, in 2007, where he is currently working toward the Ph.D. degree in the Integrated Circuit Design Group, Centre for Telematics and Information Technology.

His research interests include mixers, discrete-time systems, and phased arrays in CMOS.

Eric A. M. Klumperink (M'98–SM'06) was born in Lichtenvoorde, The Netherlands, on April 4, 1960. He received the B.Sc. degree from Hogere Technische School, Enschede, The Netherlands, in 1982 and the Ph.D. degree with a thesis entitled "Transconductance based CMOS circuits" from University of Twente, Enschede, in 1997.

After a short period in industry, he joined the Faculty of Electrical Engineering, Mathematics and Computer Science, University of Twente (UT), Enschede, in 1984, participating in analog CMOS circuit design and research. After receiving the Ph.D. degree, he started working on RF CMOS circuits. He is currently an Associate Professor with the Integrated Circuit Design Group, Centre for Telematics and Information Technology, UT. He is the holder of several patents and has authored or coauthored more than 80 journal and conference papers.

Dr. Klumperink served as an Associate Editor for the IEEE TRANSACTIONS ON CIRCUITS AND SYSTEMS—II in 2006 and 2007 and has been an Associate Editor for the IEEE TRANSACTIONS ON CIRCUITS AND SYSTEMS—I since 2008. He was a corecipient of the ISSCC 2002 Van Vessem Outstanding Paper Award.

Pieter-Tjerk de Boer was born in Wildervank, The Netherlands, in 1972. He received the M.Sc. degree in applied physics and the Ph.D. degree in computer science from the University of Twente (UT), Enschede, The Netherlands, in 1996 and 2000, respectively.

He is currently an Assistant Professor with the Design and Analysis of Communication Systems Group, Centre for Telematics and Information Technology, UT. His research interests include communication networks, their mathematical performance modeling and simulation, and rare-event simulation techniques in particular. Furthermore, he has interest in software-defined radio.

Frank E. van Vliet (M'95–SM'06) was born in Dubbeldam, The Netherlands, in 1969. He received the M.Sc. degree (with honors) in electrical engineering and the Ph.D. degree in MMIC filters from Delft University of Technology, Delft, The Netherlands, in 1992.

In 1996, he joined Netherlands Organization for Applied Scientific Research (TNO), The Hague, The Netherlands, where he is currently a Senior Technology Officer, responsible for microwave research. Since 2007, he has been a part-time Professor in microwave integration with the University of Twente, Enschede, The Netherlands. His research interests include MMIC development, advanced measurement techniques, and phased-array technology. He has authored and coauthored over 70 papers and has been involved in the definition and leading of a good number of national, EC, and military programs.

Dr. van Vliet is a member of the European Space Agency's CTB microwave board and of the European Defence Agency's Captech IAP-01.

Bram Nauta (M'91–SM'03–F'08) was born in Hengelo, The Netherlands, in 1964. He received the M.Sc. degree (*cum laude*) in electrical engineering and the Ph.D. degree, on the subject of analog CMOS filters for very high frequencies, from the University of Twente (UT), Enschede, The Netherlands, in 1987 and 1991, respectively.

In 1991, he joined the Mixed-Signal Circuits and Systems Department, Philips Research, Eindhoven, The Netherlands, where he worked on high-speed A/D converters and analog key modules. Since 1998, he has been a Full Professor with UT, where he is heading the Integrated Circuit Design Group, Centre for Telematics and Information Technology. His current research interest is high-speed analog CMOS circuits. He is also a part-time Consultant in industry. In 2001, he cofounded Chip Design Works. His Ph.D. thesis was published as a book: *Analog CMOS Filters for Very High Frequencies* (Springer, 1993).

Dr. Nauta served as an Associate Editor of the IEEE TRANSACTIONS ON CIRCUITS AND SYSTEMS—II: ANALOG AND DIGITAL SIGNAL PROCESSING from 1997 to 1999. After this, he served as a Guest Editor, an Associate Editor (2001–2006), and the Editor-in-Chief (from 2007) for the IEEE JOURNAL OF SOLID-STATE CIRCUITS. He is a member of the technical program committees of the IEEE International Solid-State Circuits Conference (ISSCC), the European Solid-State Circuits Conference, and the Symposium on VLSI Circuits. He was a corecipient of the ISSCC 2002 Van Vessem Outstanding Paper Award. He was also the recipient of the Shell Study Tour Award for his Ph.D. work. He was a Distinguished Lecturer of the IEEE and is elected member of IEEE Solid-State Circuits Society AdCom.